Available online at www.sciencedirect.com

SciVerse ScienceDirect

Acta Materialia 61 (2013) 1404–1412

Acta MATERIALIA

www.elsevier.com/locate/actamat

The relative grain boundary area and energy distributions in a ferritic steel determined from three-dimensional electron backscatter diffraction maps

Hossein Beladi [a,*], Gregory S. Rohrer [b]

[a] Institute for Frontier Materials, Deakin University, Geelong, Victoria 3216, Australia
[b] Department of Materials Science and Engineering, Carnegie Mellon University, Pittsburgh, PA 15213-3890, USA

Received 8 September 2012; received in revised form 4 November 2012; accepted 12 November 2012
Available online 10 December 2012

Abstract

The relative grain boundary area and energy distributions of a ferritic steel were characterized as a function of lattice misorientation and boundary plane orientation using focused ion beam serial sectioning combined with electron backscatter diffraction. The grain boundary energy and population depended on both the grain boundary plane orientation and lattice misorientation. When misorientation was ignored grain boundary planes with the (1 1 1) orientation had the minimum energy and the largest relative areas. The most commonly observed boundaries were {1 1 2} symmetric tilt boundaries with the Σ3 misorientation; this boundary also had a low energy. On average there was a strong inverse correlation between the relative areas of different types of grain boundaries and the relative grain boundary energies.

Keywords: Grain boundary energy; Microstructure; Ferritic steel; Electron backscattering diffraction; Focused ion beam

1. Introduction

The structure and properties of grain boundaries are of great importance because they influence diffusion [1–3], grain growth [4], strength [5,6], toughness [7,8] and creep [9] in polycrystals. Grain boundary properties are anisotropic and depend upon both the lattice misorientation and grain boundary plane orientation [10]. Because three parameters are needed to describe the lattice misorientation and two are necessary to describe the boundary plane orientation, five independent parameters must be measured to specify the properties of crystallographically distinguishable grain boundaries.

The five parameter grain boundary character distribution (GBCD) specifies the relative areas of different grain boundary types and is used as a measure of grain boundary populations. Similarly, the grain boundary energy distribution (GBED), which specifies the relative energies of different types of grain boundaries, is defined with respect to the same five macroscopic crystallographic parameters. Historically, measuring either of these quantities as a function of all five parameters was impossible because of time constraints and experimental or computational complexity. Therefore, the available results are usually restricted special grain boundaries [11–13]. However, recent advances in automated microscopy have made these measurements possible and the GBED has now been measured for a small number of materials [14–17].

In particular, the development of dual focused ion beam scanning electron microscopy in conjunction with electron backscatter diffraction (EBSD) has made it possible to precisely measure the three-dimensional (3-D) internal microstructures of material (e.g. grain boundaries) in a reasonable timeframe [18,19]. This involves extensive two-dimensional EBSD mapping coupled with automated serial

* Corresponding author. Tel.: +61 3 5227 1250; fax: +61 3 5227 1103.
E-mail address: beladi@deakin.edu.au (H. Beladi).

1359-6454/$36.00
http://dx.doi.org/10.1016/j.actamat.2012.11.017

sectioning using the ion beam. The resulting data can be used to reconstruct the three-dimensional geometry of a microstructure. These advanced techniques have recently been employed to determine the geometries of grain boundaries meeting at triple junctions and thus measure both the GBCD and GBED as a function of all five macroscopic crystallographic parameters [15,16]. So far this approach has been used to comprehensively survey the relative area and energy of grain boundaries in polycrystalline yttria [15] and nickel [16]. These measurements have shown that both the extent and characteristics of the anisotropy of GBCD and GBED vary in different materials [14–16]. In addition, a strong inverse relationship was observed between the relative population and energy of grain boundaries [15,16].

Despite the technological importance of body-centred cubic (bcc) polycrystals (e.g. ferritic steel), little is known about the grain boundary energy. The existing data were mostly calculated through advanced simulation techniques (e.g. molecular statistics simulations) [13,20–23] and those obtained experimentally are restricted to a small population of special grain boundaries [11,12]. The objective of the present paper was to provide a detailed description of the grain boundary character and energy distributions in a fully ferritic microstructure through the five parameter grain boundary analysis approach using serial sectioning combined with EBSD data.

2. Experimental procedure

2.1. Thermo-mechanical processing

The composition of steel used in the current study was 0.04 C–1.52 Mn–0.2 Si–0.22 Mo–0.08 Ti–0.033 Al (wt.%). The as-received slab, 40 mm thick, was reduced in thickness by hot rolling to 12 mm at temperatures between 1200 and 1000 °C. A cylindrical compression sample with a length of 15 mm and a diameter of 10 mm was machined out of the hot rolled plate perpendicular to the rolling direction. The sample was reheated at 5 °C s^{-1} to 1200 °C and held for 300 s. It was then cooled down to 890 °C, held for 20 s, and then deformed to a strain of 1 at a strain rate of 1 s^{-1}. Afterwards, the deformed sample was cooled to 650 °C at 10 °C s^{-1} and held for 600 s, followed by water quenching. The current thermo-mechanical procedure was employed to refine the ferrite grain size. Grain refinement was very important to obtain a high population of boundaries within the volume that can be analysed by 3-D EBSD mapping. The resultant microstructure consisted of fully polygonal ferrite grains with an average grain size of ~6 μm.

The compression device was a servo-hydraulic thermo-mechanical treatment simulator apparatus (Servotest, 500 kN) attached to an automated testing machine including an induction furnace, a muffle furnace and a computer data acquisition system. The temperature was monitored throughout the tests using a thermocouple embedded in the specimen. A boron nitride lubricant was used to coat the specimen and minimize friction between the contact surfaces of the specimen and the anvils during deformation.

2.2. 3-D EBSD measurement

A specimen was cut from the middle of the hot deformed sample along the deformation direction. Afterwards it was mechanically ground from both sides to obtain a thin strip with parallel surfaces perpendicular to the deformation direction, having a thickness of ~150 μm. 3-D EBSD measurements and serial sectioning were performed using a field emission gun Quanta 3D FEI scanning electron microscope. The thin sample was mounted on a 54° pre-tilted holder. For EBSD data collection the sample was further tilted 16° towards the EBSD detector. The 16° tilted sample was then rotated 180° towards the ion beam position to mill away a given thickness in each step. The microscope was carefully aligned to control the amount of material removed during each milling step and to ensure that the EBSD maps were collected from the same area in subsequent steps. A 40 × 40 × 150 μm pillar was made in the middle of the thin strip by Ga^+ ion milling with a 30 kV, 65 nA beam. The area perpendicular to the milling direction (i.e. 40 × 40 μm) was protected by a 1 μm thick platinum layer to minimize curtaining of the area of interest during EBSD mapping. A cross-shaped fiducial mark was then milled into the lateral surface of the pillar. The fiducial mark, in conjunction with EBS3 software, was used to automatically align the area of interest during subsequent milling and EBSD mapping steps. In each sectioning step 200 nm was removed using a 30 kV, 5 nA Ga^+ ion beam. EBSD mapping was carried out using an electron beam with a voltage of 20 kV and a current of 8 nA. The in-plane point spacing of the EBSD scans was 150 nm. The average confidence index generally varied between 0.60 and 0.70. The size of the map area was 40 × 35 μm. The present results were collected from two separate 3-D EBSD runs having a total volume of 40 × 35 × 35 μm, covering approximately 3500 grains.

2.3. Data processing

EBSD data was processed employing functions in the TSL software. First, a grain dilation clean-up function was used for all orientation maps to remove ambiguous data. A single average orientation was then assigned to all contiguous groups of similarly oriented points greater than 5 pixels (i.e. >750 nm). Boundary line traces/segments were extracted using the grain boundary reconstruction function and employing a boundary deviation limit of two pixels (i.e. 300 nm). Boundary segments less than 450 nm were excluded from the analysis. The resulting line traces were then employed to calculate the five parameter grain boundary character and energy distributions using

a procedure described in detail elsewhere [15]. Briefly, triple points where three line segments meet were identified. The orientations of the grains around the triple points were then compared with triple points with a similar location on adjacent layers. When two triple points on adjacent layers were made up of crystals with the same orientation they were connected to construct a triple line. The current dataset yielded approximately 32,000 triple lines. The cross-product of the triple line connecting adjoining layers and the corresponding grain boundary line trace gives the grain boundary normal vector (i.e. grain boundary plane orientation). This calculation generated approximately 192,000 normal vectors.

Two sources of uncertainty arise from the discrete nature of the data and the serial sectioning process. One is the relative in-plane (i.e. horizontal) and between plane (i.e. vertical) resolution. The other is the horizontal alignment of the layers. These uncertainties were examined in Rohrer et al. [17] and it was found the first could be reduced by connecting the triple lines between alternate layers so that the vertical discretization becomes coarser than the horizontal discretization. The second uncertainty was reduced by using a sub-pixel alignment procedure that rigidly shifts layers so that the mean of the triple line direction distribution is normal to the surface of the sample. In most instances the adjustment is less than one pixel spacing [15].

The grain boundary energy calculation was performed using the capillarity vector reconstruction method established by Morawiec [24]. Similarly to most interface energy measurements, the capillarity vector reconstruction method employs observations of the interfacial geometry and the assumption that the triple junction is in local thermodynamic equilibrium. Under these conditions the grain boundary energy is related to the interfacial geometry through the Herring [25] equation. In the capillarity vector reconstruction method the Hoffman and Cahn [26,27] formulation of the Herring equation is used: $(\zeta^1 + \zeta^2 + \zeta^3) \times 1 = 0$. Here ζ^1, ζ^2 and ζ^3 are the capillarity vectors associated with the three grain boundaries and 1 is the triple line. Each capillarity vector has one component perpendicular to the grain boundary and another component tangential to the boundary. The scale of the first component is equal to the relative grain boundary energy. The magnitude of the second component represents the differential of the energy with respect to a right-handed rotation about 1.

In the current study the GBCD and GBED were discretized with nine bins per 90° using procedures described in detail elsewhere [15]. At this level of discretization 97% of the bins contained at least 10 observations. The energy reconstruction was carried out on 32,000 triple junctions. The capillarity vector reconstruction method is iterative, as explained in Morawiec [24]. In this case 300 iterations were used and the relaxation factor for each iteration was 0.034. The change on the last iteration was less than 1% of the change on the first, which was taken as a condition for convergence.

3. Results

Fig. 1 shows a constructed 3-D EBSD map for 68 parallel layers. The microstructure consisted of two ferrite grain size populations: (i) regions with several closely spaced arrays of very fine ferrite grains in the range 1–5 μm; (ii) coarse grains having a size between 5 and 15 μm, mainly enclosed by fine grains. This is a result of an inhomogeneous distribution of strain in the hot deformed prior austenite grain structure. The strain mostly concentrated in the vicinity of prior austenite grain boundaries rather than grain interiors during deformation, resulting in an inhomogeneous distribution of nucleation sites. Therefore, the fine grains were most likely nucleated in the vicinity of prior austenite grain boundaries, where the highest density of ferrite nucleation sites exists. This led to full impingement of ferrite grains at an early stage of phase transformation, resulting in very limited coalescence of the ferrite grains on cooling. In contrast, there were fewer ferrite nucleation sites at the prior austenite grain interiors, leading to the nucleation of fewer ferrite grains and, consequently, a coarser ferrite grain size. The fully ferritic microstructure revealed a prominent γ-fibre ⟨1 1 1⟩‖ND crystallographic texture and a weak presence of (1 1 3)[1 −1 0], (1 1 0)[1 −1 0], (0 0 1)[1 −1 0] and (0 0 1)[0 −1 0] components; the overall maximum was 3.87 times random (Fig. 2a). The inverse pole figure was characterized by a relatively weak texture with a maximum of 3.13 times random intensity (Fig. 2b), with stronger (1 1 1) and (1 1 0) fibres oriented along the normal direction.

The distribution of grain boundary planes independent of misorientation, $\lambda(n)$, where n is the normal to the grain boundary, was nearly isotropic, having a maximum at the (1 1 1) position with a value of 1.05 multiples of a random distribution (MRD). In other words, the population is 5% greater than expected in a random distribution. The

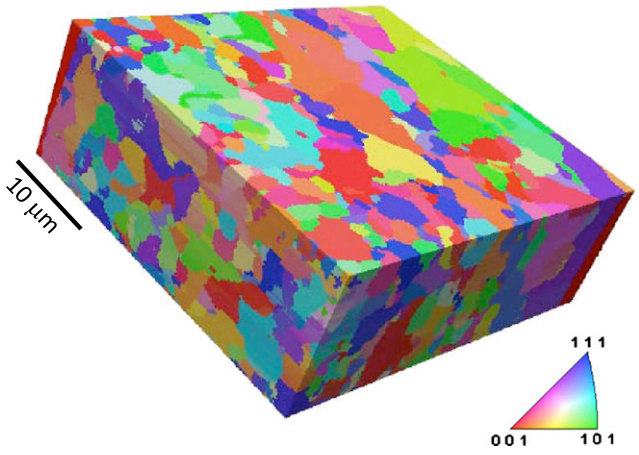

Fig. 1. Reconstructed serial sections of electron backscatter diffraction data for the ferritic structure containing 68 slices. The colours are the orientations referred to the normal direction. (For interpretation of the references to colour in this figure legend, the reader is referred to the web version of this article.)

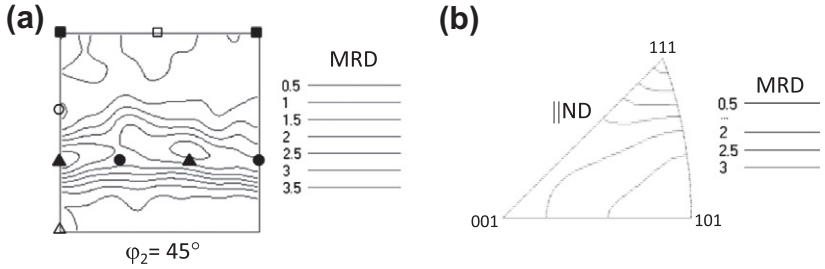

Fig. 2. (a) Orientation distribution function of the ferritic steel and (b) inverse pole figure of the steel along the normal direction. The MRD is multiples of a random distribution. ■{001}⟨110⟩; ●{111}⟨112⟩; ▲{111}⟨110⟩; □{001}⟨010⟩; ○{113}⟨110⟩; △{110}⟨110⟩.

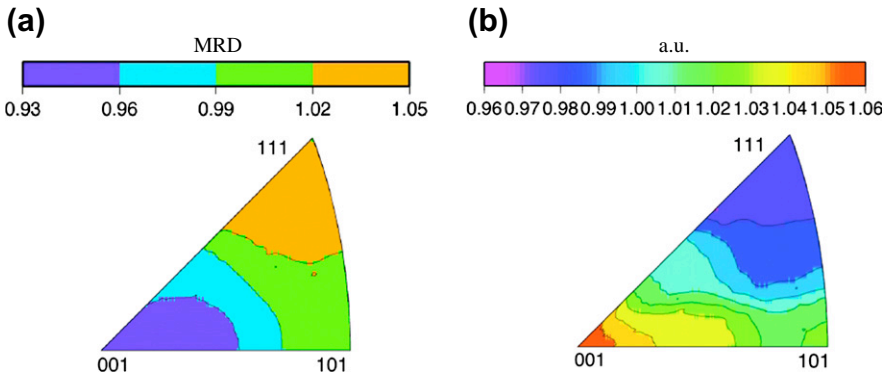

Fig. 3. The distribution of (a) grain boundary planes and (b) energy of the ferritic steel. a.u., arbitrary unit.

minimum of the distribution was centred at (100), with 0.93 MRD (Fig. 3a). The distribution was ~1 MRD at the (101) position. Similarly, the relative grain boundary energy as a function of grain boundary plane orientation revealed a weak anisotropy. However, the energy distribution maxima and minima were inversely correlated with the relative area distribution, centring at (100) with 1.06 a.u. and (111) with 0.96 a.u., respectively (Fig. 3b). The energy at (101) was ~1.01 a.u.

The grain boundary plane distribution for specific misorientations, λ ($n|\omega/(uvw)$), was plotted as a stereographic projection to examine the distribution of grain boundary planes in the bi-crystal reference frame. Here the [001] crystal axis is positioned perpendicular to the page and the [100] direction points horizontally in the plane of the paper and to the right. In the present study the grain boundary plane distribution was plotted for misorientations about the [111], [110] and [100] axes. Specific coincident site lattice (CSL) misorientations (Σ1, Σ3, Σ5, Σ7, Σ9, Σ11, Σ13, Σ17, Σ19 and Σ21) were selected as typical examples of the distributions. The grain boundary plane distributions varied significantly as a function of misorientation. For example, for misorientations about the [111] axis there was a peak at the (111) twist position that decreased as the misorientation angle increased from 10° (Σ1, Fig. 4a) to 38° (Σ7, Fig. 5c). At larger angles a minimum was found at the twist orientation and the maxima were at the (112) symmetric tilt positions with a relatively high population spread along the zone of tilt boundaries (see Fig. 4b, Σ3). The {211}‖{211} symmetric tilt grain boundaries are coherent twins for the Σ3 misorientation in bcc materials [28], and these boundaries formed the largest population in the distribution, which was approximately 13 MRD. There was also a relatively high population at the (110) symmetric tilt positions, i.e. the closest packed plane in bcc materials, with ~8 MRD. In contrast, there was a minimum in population (but still more than twice random) centred at the position of (111)‖(111) pure twist boundaries, which are the coherent twin boundaries in face-centred cubic (fcc) metals [10]. Similar conclusions were reached in a recent two-dimensional study of an IF steel [29].

Similar to the GBCD, the relative grain boundary energy distribution for [111] type misorientations varied as a function of the misorientation angle (Figs. 4c, d and 5e–h). However, the positions of the maxima and minima were inversely correlated with the corresponding GBCD for all misorientation angles (Figs. 4 and 5). In other words, the grain boundaries with the highest populations appeared to have the minimum energy and the grain boundaries with the minimum energy were most frequently populated. For instance, the minimum energy appeared at the position of the (112) symmetric tilt boundaries (i.e. the coherent twin boundary for bcc) at a misorientation angle of 60° (i.e. Σ3, Fig. 4d). This agrees well with the positions with the maximum population in the corresponding GBCD (Fig. 4b and d). Similar correlations were obvious for other misorientations about the [111] axis, where the twist

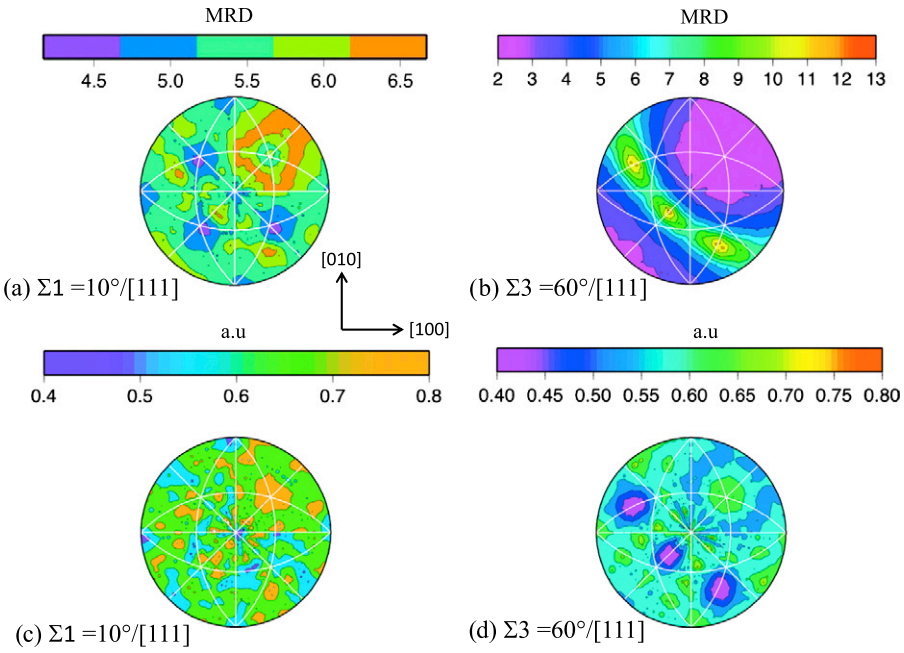

Fig. 4. (a, b) The distribution of grain boundary planes and (c, d) the corresponding grain boundary energy distribution at fixed misorientations of 10°/[1 1 1] and 60°/[1 1 1], respectively, plotted in stereographic projection along [0 0 1].

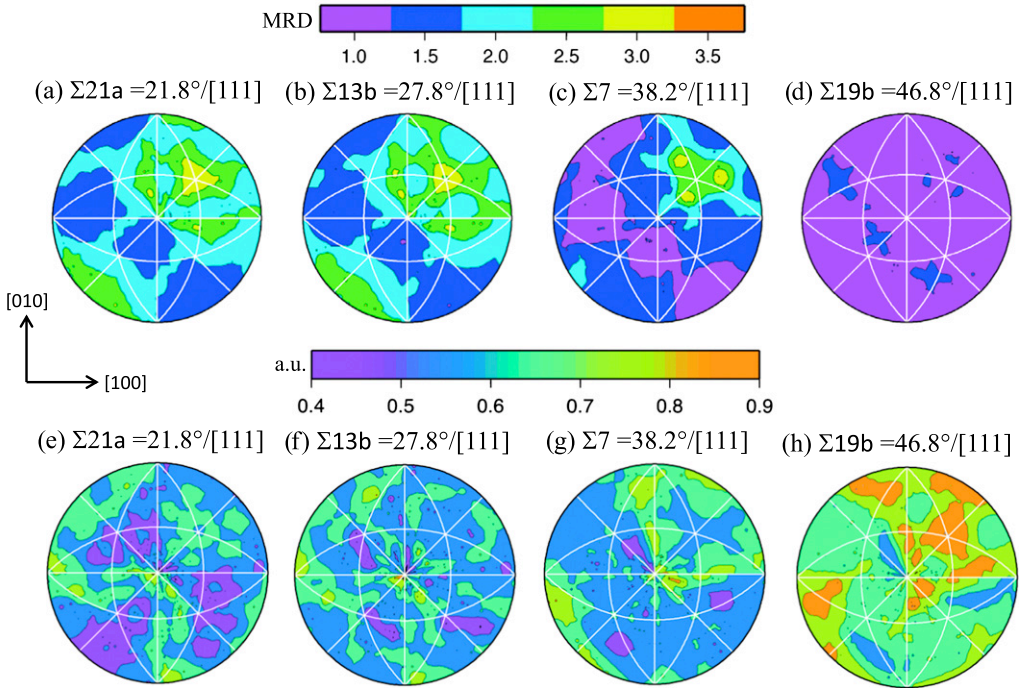

Fig. 5. (a–d) The distribution of grain boundary planes and (e–h) the corresponding grain boundary energy distribution at fixed misorientations of 21.8°/[1 1 1], 27.8°/[1 1 1], 38.2°/[1 1 1] and 46.8°/[1 1 1], respectively, plotted in stereographic projection along [0 0 1].

position has a relatively low energy (e.g. Σ7, Fig. 5). Note that the Σ19b grain boundary had the highest energy (averaged over all planes) and also had the lowest average population (Fig. 5d and h).

The distribution of grain boundary planes with a 38.9° misorientation about the [1 0 1] axis had modest maxima (~1.6 MRD) at {1 1 0}‖{1 1 0} twist boundaries and {2 2 1}‖{2 2 1} symmetric tilt boundaries. The symmetric tilt boundaries were on the great circle perpendicular to [1 1 0] (Fig. 6a). However, the energy distribution did not have an obvious inverse correlation with the populations for the Σ9 boundary. For example, the peak energy was observed at

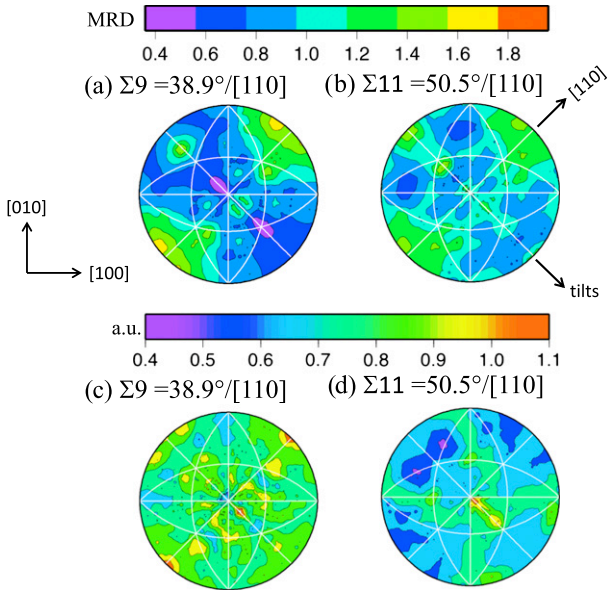

Fig. 6. (a, b) The distribution of grain boundary planes and (c, d) the corresponding grain boundary energy distribution at fixed misorientations of 38.9°/[1 1 0] and 50.5°/[1 1 0], respectively, plotted in stereographic projection along [0 0 1].

the {1 1 0} twist boundary, which also had the highest population (Fig. 6a and c). There was a slight change in the peak distributions when the misorientation angle increased to 50.5°. Although the twist boundaries still appeared at a misorientation angle of 50.5°, the position of the maxima on the tilt boundary zone axis moved closer to the {1 1 1} symmetric tilt boundaries (i.e. Σ11, Fig. 6b). The energy distribution showed the expected inverse correlation with the population, with minima at the positions of {1 1 1} symmetric tilt boundaries and {1 1 0} twist boundaries (Fig. 6d).

The major characteristic of the grain boundaries with [1 0 0] misorientations was that they occurred relatively infrequently (Fig. 7). Only a few grain boundary plane orientations for Σ13a had populations that exceeded 1 MRD, and for the Σ17a and Σ5 all of the populations were less than or equal to 0.7 MRD. For the Σ13a boundary the two most populated boundaries were the {1 0 0} twist boundary and the (0 1 2)‖(0 1 2) symmetric tilt boundary. The symmetric tilt boundary was found on the vertical great circle in the centre of the stereogram (see Fig. 7a). For higher misorientation angles the populations were much lower. The grain boundary energy distributions showed an inverse correlation, as noted for other misorientations. Note that the average energy of the Σ17a and Σ5 misorientations were larger than for Σ13a and, overall, there were many fewer of these grain boundaries.

The average relationship between the grain boundary population and energy is illustrated in Fig. 8. Here the grain boundary energies were classified into equally spaced bins with a width of 0.025 a.u., and the average population of all boundaries in a given bin was calculated. Even though points in the five-dimensional space can be identified where the inverse correlation is not obvious

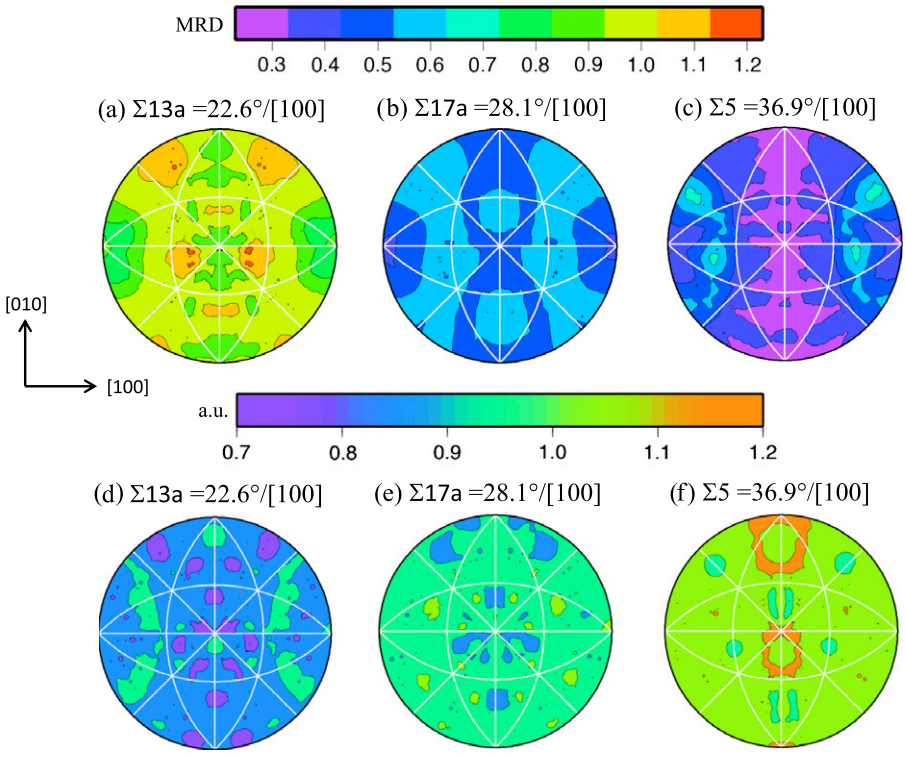

Fig. 7. (a–c) The distribution of grain boundary planes and (d–f) the corresponding grain boundary energy distribution at fixed misorientations of 22.6°/[1 0 0], 28.1°/[1 0 0] and 36.9°/[1 0 0], respectively, plotted in stereographic projection along [0 0 1].

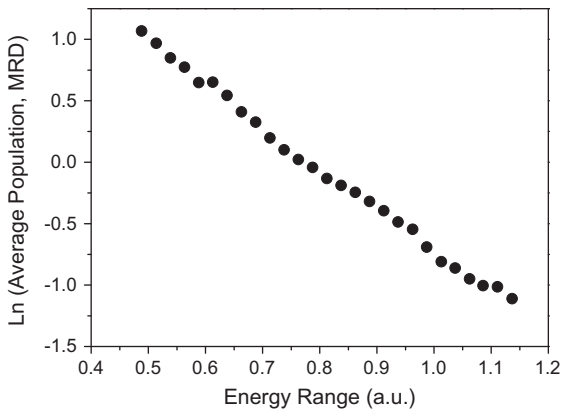

Fig. 8. The average relationship between the grain boundary population and energy. The grain boundary energies were classified into equally spaced bins with a width of 0.025 a.u.

(for example for the Σ9 boundary in Fig. 6a and b), the average result shown in Fig. 8 illustrates a very strong inverse correlation between the grain boundary population and the relative grain boundary energy.

4. Discussion

The data presented here results from the first comprehensive study of the grain boundary energy distribution of a ferritic steel over all five crystallographic parameters. The energy measurements were coupled with simultaneous measurements of the grain boundary character distribution. The findings differ substantially from those for fcc metals (e.g. Ni and Cu [30]), whose grain boundary populations are dominated by twins and boundaries that result from interactions among twins. The population of Σ3 boundaries in a fcc metal may be in the range 10–50% of the total boundary area, while they make up only ~2.5% of the total grain boundary area in the ferritic material examined here. This is very close to the Σ3 population (~3%) recently reported in an IF steel that also had a bcc structure [29]. This is not surprising, as multiple twinning is not expected to occur during the evolution of a bcc microstructure [8].

One of the most interesting results of the current investigation is a strong inverse relationship between the grain boundary population and grain boundary energy (Fig. 8). While there are certain population and energy bins that are not well correlated (e.g. Σ9, Fig. 6a and c), Fig. 8 demonstrates that on average the logarithm of the population has a strong inverse correlation with the grain boundary energy. A similar relationship was reported from experimental measurements of other materials with different crystal structures [14,15,31] and later supported by simulations [32–34]. It has been shown that random interactions among growing grains, and the biased annihilation of higher energy boundaries as grains disappear during grain growth, leads to this Boltzmann-like distribution [35]. In previous studies of Ni there were significant deviations from a linear relation between ln(population) and energy, presumably because of non-random interactions among twins. The more isotropic distribution in this material has a more ideal linear dependence, as found in the various simulations [32–35].

In the current study the grain boundary plane dependence of the grain boundary energies, independent of misorientation, was relatively isotropic. The grain boundary populations in the crystal reference frame, independent of misorientation, was also nearly isotropic (see Fig. 3). A similar distribution has recently been reported for an IF steel [29]. While the shapes of the distributions are consistent, there was much more anisotropy in the IF steel. The current result is not, however, consistent with the grain boundary distribution for a Fe–1% Si steel, in which the grain boundaries were more frequently terminated by {1 1 0} planes and the minimum population was centred about the {1 1 1} planes [36].

There are two principal factors that strongly influence the grain boundary population. One is the grain boundary energy and the second is texture. As noted above, the grain boundary population in a random microstructure is expected to be inversely correlated with the grain boundary energy. Alloys with different additives that alter the grain boundary energy are therefore expected to have different grain boundary energies. While we do not have grain boundary energy data for Fe–3% Si steel, there is some data on the surface energies. Considering the fact that a grain boundary is formed by two joined surfaces, the surface energies should correlate with the grain boundary energies [14]. Gale et al. [20] showed that the temperature strongly influences the surface energy of a Fe–3% Si steel, altering the plane with the minimum surface energy. The variation in the surface energy with temperature was described through the extent of silicon/oxygen absorption on planes. In contrast, another study argued that the (1 1 1) surface has minimum energy in Fe–3% Si and textures that expose more of this surface, such as $(1\,1\,1)\langle u\,v\,w\rangle$, are favored during recrystallization because of this energy advantage [11]. The current result is consistent with the latter conclusion [11], as the ferritic structure has a (1 1 1)||ND texture, similar to the IF steel [29], revealing the maximum population and minimum energy both centred on the {1 1 1} planes (Fig. 3). The IF steel, though, had much stronger (1 1 1) fibres oriented along the normal direction (i.e. 8.8 times random [29]) compared with the current result (i.e. 3.13 times random). This orientation preference leads to a non-uniform distribution of misorientations; the effect on the grain boundary plane distribution is more difficult to predict. The difference between the current grain boundary plane distribution and the distributions reported for other bcc crystal structures could arise from differences in both the texture and/or the alloy composition and its effect on the grain boundary energy. Further investigation will be needed to understand the relative contributions of each factor.

The distribution of grain boundary normals at a given lattice misorientation in this ferritic microstructure differs significantly from those reported for fcc materials [16,30,37]. For instance, at the $\Sigma3 = 60°/[1\,1\,1]$ misorientation the grain boundaries in fcc materials are mostly pure twist, but in ferrite symmetric tilt boundaries dominate the population. Furthermore, the total anisotropy at this misorientation is much smaller in ferrite. The $\Sigma9$ and $\Sigma11$ misorientations are also examples. In fcc materials these misorientation are dominated by tilt boundaries, while in ferritic steel twist boundaries have high populations. The one misorientation where the grain boundary plane distributions are similar in the two crystal structures is at $\Sigma7 = 38.2°/[1\,1\,1]$. In this case pure twist boundaries dominate the distribution in both bcc (Fig. 5c) and fcc structured materials [30,31,37]. These data show that the distribution of grain boundary normals at specific lattice misorientations is strongly influenced by the crystal structure. Considering that the grain boundary population is inversely correlated with its energy, the differences in the grain boundary plane distributions are presumably the result of differences in the grain boundary energy distributions. The $\Sigma3$ boundary, for instance, shows the maximum population along the zone of tilt boundaries (i.e. $\{1\,1\,2\}$ planes) and minima at the position of the pure twist $\{1\,1\,1\}$ plane, and these positions also represent the lowest and highest energies, respectively, at this misorientation (Fig. 4b and d). This is indeed consistent with the experimental measurements [12] and recent simulations [21–23] confirming that the $\{1\,1\,2\}$ twin grain boundary plane in the bcc structure has a much lower energy compared with the $\{1\,1\,1\}$ plane. Materials with the fcc structure, on the other hand, show a completely opposite grain boundary population/energy distribution, where, for the $\Sigma3$ boundary, $\{1\,1\,1\}$ planes having the lowest energy and being the most populous [16]. A similar phenomenon can be observed for the $\Sigma11$ boundary, where the twist and symmetric tilt boundaries are most populated for bcc (Fig. 6b) and fcc crystal structures [37], respectively, because of differences in the low energy grain boundary planes.

To draw a comparison with previous calculations, we can extract the energies of the symmetric $\langle 1\,1\,0\rangle$ tilt boundaries, which are compared with the populations in Fig. 9. In interpreting this data and making a comparison two factors must be recognized. First, the resolution in the energies computed by simulation is much higher than the results of our energy reconstruction, where the bin size is approximately 10°. Second, non-physical discontinuities (noise) can appear in the reconstructed energies because of the discretization. When the energy for a specific grain boundary is computed from the reconstructed energies (for example each of the points in Fig. 9) all symmetrically equivalent bins that contain the boundary are averaged to obtain the result. Depending on where the grain boundary is in crystallographic space with respect to the boundaries between bins there can be discontinuous changes over small angular intervals. For example, the steep drop and rise around $\Sigma19/(3\,3\,1)$, producing an apparent cusp, must be non-physical because the three points are only separated by 9°, less than the size of a bin. Acknowledging these limitations, we can compare Fig. 9 with the results in Nakashima and Takeuchi [21] and Tschopp et al. [23]. The calculations by Nakashima and Takeuchi [21] and Tschopp et al. [23] agree with each other that there is a large cusp at $\Sigma3/(1\,1\,2)$ and a smaller one at $\Sigma11/(3\,3\,2)$. Our reconstructed energies also suggest a cusp at the $\Sigma3/(1\,1\,2)$ position and that the energy of the $\Sigma11/(3\,3\,2)$ boundary is in a broad local minimum that also includes $\Sigma3/(1\,1\,1)$. Note that the $\Sigma3/(1\,1\,1)$ boundary is not predicted to have a significantly low energy by the calculations [21,23]. Therefore, some aspects of the reconstructed energies are consistent with the simulations and others are not. Unfortunately, the current resolution of experimentally determined energies does not support a detailed comparison with the available calculations. It should be noted that a recent comparison between reconstructed and computed grain boundary energies in Ni indicated that agreement was excellent for the boundaries that were frequently observed and, therefore, had an adequate statistical representation in the data [38].

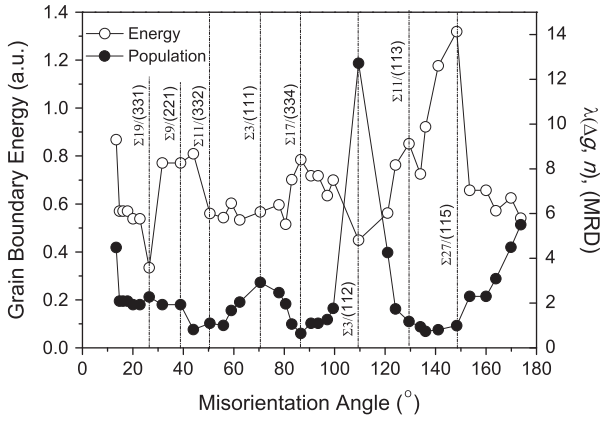

Fig. 9. Comparison of the measured grain boundary energy with population as a function of symmetric [1 1 0] tilt boundary misorientation angle.

5. Conclusion

The 3-D interfacial grain boundary network in ferritic steel was investigated as a function of five macroscopic crystallographic parameters using EBSD mapping in conjunction with focused ion beam serial sectioning. The relative grain boundary area and energy distributions depended upon both the grain boundary plane orientation and the lattice misorientation. Grain boundaries terminated by (1 1 1) planes had relatively lower energies and higher populations in comparison with other boundaries. The most frequently observed grain boundaries were $\{1\,1\,2\}$ symmetric tilt boundaries with the $\Sigma3$ misorientation. These symmetric tilt boundaries also had the lowest energy at this misorientation. On average there was a

strong inverse correlation between the relative areas and the relative grain boundary energies in ferrite.

Acknowledgements

The work at Deakin University was supported through grants provided by the Australian Research Council. H.B. is also grateful for financial assistance granted by the Outside Study Program of Deakin University. Financial support at Carnegie Mellon from the ONR-MURI under the Grant No. N00014-11-1-0678 is gratefully acknowledged. Support for facilities by the MRSEC program of the National Science Foundation under award DMR-0520425 is also acknowledged.

References

[1] Watanabe S, Takamatsu Y, Sakaguchi N, Takahashi H. J Nucl Mater 2000;152:283.
[2] Dollar M, Gleiter H. Scripta Metall 1985;481:19.
[3] Lejcek P, Hofmann S, Paidar V. Acta Mater 2003;51:3951.
[4] Humphreys FJ, Hatherly M. Recrystallization and related annealing phenomena. 2nd ed. Oxford: Elsevier; 2004.
[5] Hall EO. Proc Phys Soc Lond 1951;B64:747.
[6] Petch NJ. J Iron Steel Inst 1953;174:25.
[7] Lim LC, Watanabe T. Scripta Metall 1989;23:489.
[8] Watanabe T, Fuji H, Oikawa H, Arai KI. Acta Metall 1989;37:941.
[9] Coble RL. J Appl Phys 1963;34:1679.
[10] Rohrer GS, Saylor DM, El Dasher B, Adams BL, Rollett AD, Wynblatt P. Z Metallkd 2004;95:197.
[11] Mee PB. Trans Metall Soc AIME 1968;242:2155.
[12] Dunn CG, Daniels FW, Bolton MJ. J Metals Trans AIME 1950;188:368.
[13] Wolf D, Phillpot S. Mater Sci Eng A 1989;107:3.
[14] Saylor DM, Morawiec A, Rohrer GS. Acta Mater 2003;51:3663.
[15] Dillon SJ, Rohrer GS. J Am Ceram Soc 2009;92:1580.
[16] Li J, Dillon SJ, Rohrer GS. Acta Mater 2009;57:4304.
[17] Rohrer GS, Li J, Lee S, Rollett AD, Groeber M, Uchic MD. Mater Sci Technol 2010;26:661.
[18] Uchic MD, Groeber MA, Dimiduk MD, Simmons JP. Scripta Mater 2006;55:23.
[19] Konrad J, Zaefferer S, Raabe D. Acta Mater 2006;54:1369.
[20] Gale B, Hunt RA, McLean M. Philos Mag 1972;25:947.
[21] Nakashima H, Takeuchi M. Testu-to-Hagane 2000;86:357.
[22] Kim HK, Ko WS, Lee HJ, Kim SG, Lee BJ. Scripta Mater 2011;64:1152.
[23] Tschopp MA, Solanki KN, Gao F, Sun X, Khaleel MA, Horstemeyer MF. Phys Rev B 2012;85:1.
[24] Morawiec A. Acta Mater 2000;48:3525.
[25] Herring C. Surface tension as a motivation for sintering. In: Kingston WE, editor. The physics of powder metalurgy. New York: McGraw-Hill; 1951. p. 143–79.
[26] Hoffman DW, Cahn JW. Surf Sci 1972;31:368.
[27] Cahn JW, Hoffman DW. Acta Metall 1974;22:1205.
[28] Hirth JP, Lothe J. Theory of dislocations. 2nd ed. Malabar, FL: Krieger Publishing Co.; 1982. p. 366.
[29] Beladi H, Rohrer GS. Metall Mater Trans A, in press. doi: http://dx.doi.org/10.1007/s11661-012-1393-0.
[30] Randle V, Rohrer GS, Miller HM, Coleman M, Owen GT. Acta Mater 2008;56:2363.
[31] Saylor DM, Morawiec A, Rohrer GS. Acta Mater 2003;51:3675.
[32] Gruber J, George DC, Kuprat AP, Rohrer GS, Rollett AD. Scripta Mater 2005;53:351.
[33] Rohrer GS, Gruber J, Rollett AD. In: Rollett AD, editor. Applications of texture analysis. Hoboken, NJ: J. Wiley & Sons; 2009. p. 343.
[34] Gruber J, Rohrer GS, Rollett AD. Acta Mater 2010;58:14.
[35] Dillon SJ, Rohrer GS. Acta Mater 2009;57:1.
[36] Bennett TA, Kim CS, Rohrer GS, Rollett AD. Mater Sci Forum 2004;467–470:1057.
[37] Saylor DM, El Basher BS, Rollett AD, Rohrer GS. Acta Mater 2004;52:3649.
[38] Rohrer GS, Holm EA, Rollett AD, Foiles SM, Li J, Olmsted DL. Acta Mater 2010;58:5063.